# Activation and Proton Transport Mechanism in Influenza A M2 Channel

Chenyu Wei[†‡*] and Andrew Pohorille[†‡*]
[†]NASA Ames Research Center, Moffett Field, California; and [‡]Department of Pharmaceutical Chemistry, University of California, San Francisco, San Francisco, California

ABSTRACT Molecular dynamics trajectories 2 $\mu$s in length have been generated for the pH-activated, tetrameric M2 proton channel of the influenza A virus in all protonation states of the pH sensor located at the $His^{37}$ tetrad. All simulated structures are in very good agreement with high-resolution structures. Changes in the channel caused by progressive protonation of $His^{37}$ provide insight into the mechanism of proton transport. The channel is closed at both $His^{37}$ and $Trp^{41}$ sites in the singly and doubly protonated states, but it opens at $Trp^{41}$ upon further protonation. Anions access the charged $His^{37}$ and by doing so stabilize the protonated states of the channel. The narrow opening at the $His^{37}$ site, further blocked by anions, is inconsistent with the water-wire mechanism of proton transport. Instead, conformational interconversions of $His^{37}$ correlated with hydrogen bonding to water molecules indicate that these residues shuttle protons in high-protonation states. Hydrogen bonds between charged and uncharged histidines are rare. The valve at $Val^{27}$ remains on average quite narrow in all protonation states but fluctuates sufficiently to support water and proton transport. A proton transport mechanism in which the channel, depending on pH, opens at either the histidine or valine gate is only partially supported by the simulations.

## INTRODUCTION

The M2 proton channel of the influenza A virus is a transmembrane protein assembly that conducts protons across the viral envelope to acidify the interior of the viron when the external pH drops below ~6.5 (1–4). Considering that this is a required step for invading the host and subsequent replication of the virus (5,6), understanding the mechanism of proton transport and its relation to the channel structure might be helpful for designing efficient antiflu drugs. The M2 protein, which is composed of 96 residues, associates to form homotetrameric structures, but much shorter constructs containing the helical transmembrane segments retain most properties of the native channel (7–10).

M2 is not only one of the smallest ion channels but also one of the most studied. A number of its properties, such as structure (11,12), conduction rates, and specificity (2,4,13–17), and effects of mutations on function (17–21), have been extensively investigated. Among transmembrane residues of the protein, $His^{37}$, which resides near the center of the channel facing the lumen, has been found to play the role of pH sensor (18,20). Its pKa of 6.1 in aqueous solution is close to a pH that activates the channel. Physiological studies have shown that mutations of $His^{37}$ abolish pH sensitivity of the channel (18,20). Several other residues lining the lumen, such as $Val^{27}$ (17,21) and $Trp^{41}$ (19), have also been shown to play important roles in proton transport (see Fig. 1). The tetrad of $Val^{27}$ forms a valve on the extracellular side of the pore, whereas $Trp^{41}$ forms a constriction on the outgoing side of the $His^{37}$ box that opens up at low pH.

In recent years, several x-ray, solution NMR, and solid-state NMR (ssNMR) structures of M2 have become available, greatly advancing our molecular-level understanding of proton transport and gating in the channel. These structures include 1), a high-resolution x-ray structure (Protein Data Bank (PDB) ID 3LBW) at pH 6.5 (22), 2), lower-resolution x-ray structures at pH 7.5 (PDB ID 3BKD) and 5.3 (PDB ID 3C9J) (23), 3), a solution NMR structure (PDB ID 2RLF) at pH 7.5 (24), and 4), an ssNMR structure (PDB ID 2L0J), also at pH 7.5 (25), and are listed in Table S1 in the Supporting Material. NMR structures of an M2 mutant (26) and M2 in the presence of the drug rimantadine (27) have also been published. However, despite this wealth of structural data, the mechanism of proton transport and gating remains elusive.

Several mechanisms have been proposed to explain structural and functional data. They roughly fall into two main categories, involving either a shutter (28) or a shuttle (11) mechanism. In the former, protons are transported through a continuous water wire by way of a Grotthuss-type mechanism (29,30) when electrostatic repulsion between $His^{37}$ residues that become charged at low external pH causes the channel to open. The shutter mechanism has been extensively investigated in molecular dynamics (MD) simulations (28,31–36), but the calculated proton conductance (37) was found to be orders of magnitude higher than that measured experimentally (2,4,13–17). In the shuttle mechanism, the proton transport path directly involves $His^{37}$. A proton acquired by this residue from the extracellular side is released to the intracellular side. This mechanism was first proposed by Pinto et al. (11) to account for experimental observations that M2 is highly proton-selective (2,4,14) and that its conduction rate saturates at low pH (2,4,14,17). These observations cannot be readily explained by the shutter mechanism.

*Submitted March 12, 2013, and accepted for publication August 8, 2013.*
*Correspondence: chenyu.wei@nasa.gov or andrew.pohorille@nasa.gov
Editor: Gerhard Hummer.

0006-3495/13/11/2036/10 $2.00
http://dx.doi.org/10.1016/j.bpj.2013.08.030

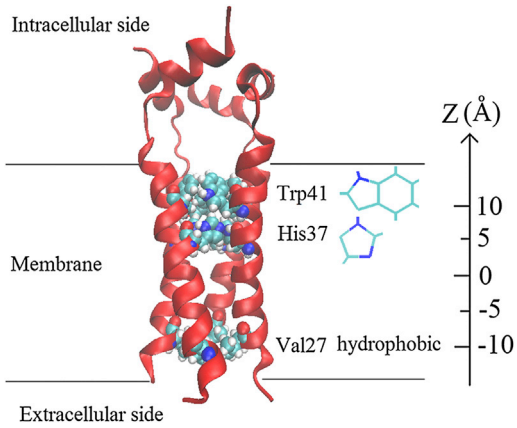


FIGURE 1 Atomic structure of M2 from the solution NMR experiment (PDB ID 2RLF). The functionally important residues $Val^{27}$, $His^{37}$, and $Trp^{41}$ are marked. The normal direction ($z$) of the host membrane is also labeled. To see this figure in color, go online.

Furthermore, a higher-than-usual deuterium effect on proton conductance (4) also suggests that proton transport might proceed through a path other than a water wire. Using a transition-state model, Lear showed that progressive protonation of $His^{37}$ could reproduce the saturation effect observed experimentally (38). Schweighofer and Pohorille investigated the shuttle mechanism in MD simulations of the transmembrane segment of M2 at different protonation states (39). In those simulations, the channel became unstable when more than two $His^{37}$ residues were protonated.

A number of important issues related to proton transport still remain unclear. Several are related to protons passing through the $His^{37}$-$Trp^{41}$ cluster. The shuttle mechanism, as originally proposed by Pinto et al. (11) and studied in MD simulations by Schweighofer and Pohorille (39), involves conformational changes in histidine residues. Recent ssNMR studies (40,41) lend support to this mechanism, as they have shown strong hydrogen binding between $His^{37}$ and water and suggest interconversion between conformational states of $His^{37}$. Other ssNMR studies (25), however, yield a different picture. From these studies, it has been concluded that when two residues in the $His^{37}$ tetrad are protonated, each proton is shared between two adjacent histidines, thus participating in a strong hydrogen bond. In this protonation state, the tetrad locks the $His^{37}$-$Trp^{41}$ cage in the closed state and proton exchange with neighboring waters is unlikely. Only when pH drops sufficiently for the third histidine in the tetrad to be protonated, thus breaking one strong hydrogen bond, does the tetrad become capable of shuttling protons. The mechanism of opening the constriction at $Trp^{41}$ is also not well established, and it might involve local deformation of the protein backbone or reorientation of the indole ring. The $Val^{27}$ valve on the extracellular side of the $His^{37}$-$Trp^{41}$ cage might also play an important role in transport. On the basis of the comparison between structures obtained at different pH values, it has been proposed that proton transport is associated with large, proton-induced helical displacements, with the channel alternatively opening at $Val^{27}$ or $His^{37}$ at neutral and low pH (22,42).

Contributing to the difficulties in determining the mechanism of proton transfer is the inability to assign unambiguously protonation states of $His^{37}$ residues as a function of pH. Structures obtained in x-ray or NMR experiments do not provide direct information on this issue, because positions of hydrogen atoms are not determined in these experiments. In the heterogeneous environment in the channel lumen, the pKa of $His^{37}$ could differ from that in bulk water. Adding to the complications, $His^{37}$ residues in the M2 tetramer could be protonated individually and progressively. This yields five different protonation states of $His^{37}$ in the channel. There are discrepancies in experiments regarding the exact pKa values of these histidines. Early work by Okada et al. (43) yielded a pKa value at 5.7 and a second at $<4$ from UV resonance Raman spectroscopy. In a later ssNMR study, Hu et al. (44) measured pKa values of 8.2, 8.2, 6.3, and $<5$ for the first, second, third, and fourth protonation states, respectively. This means that two $His^{37}$ residues are doubly protonated even at neutral pH, which is unexpected given the close distance between the charges on the $His^{37}$ residues. Considering that the activation pH is close to 6.5, the channel conducts protons when at least three $His^{37}$ residues are protonated. This is in very good agreement with kinetic measurements that yield the two lowest pKa values of 6.25 and 4.7 (17). However, a recent ssNMR experiment by Hu et al. (41), with a different method for extracting pKa, yielded lower pKa values of 7.6, 6.8, 4.9, and 4.2. This means that the channel might be active even when only two histidines are doubly protonated.

The primary goal of this work is to evaluate different mechanisms of proton transport and gating by way of MD simulations. Proton transport is quantum mechanical in nature, and therefore, direct investigations of this process require an approach that combines quantum and statistical methods. At present, such an approach cannot be applied in sufficiently long computer simulations. For this reason, we instead simulate the channel at all possible protonation states of the histidine box using classical MD at microsecond timescales and exploit the fact that different hypotheses about the mechanism of transport have different structural implications. In combination with x-ray and NMR studies, which provide frozen snapshots and averaged structures, respectively, the presence of water wires through the $His^{37}$ gate, the dynamics and hydrogen bonding of histidines, the conformation of $Trp^{41}$, water transport through the $Val^{27}$ valve, and large-scale motions of M2 helices as functions of the protonation state of $His^{37}$ are probed in MD simulations. They inform us about the most likely mechanism through which protons transverse the channel and how the process is gated at different locations along the lumen.

## METHODS

The M2 channel was embedded in a 1-palmitoyl-2-oleoylphosphatidylcholine (POPC) membrane with water lamellae on both sides. The simulation unit cell of 72.8 × 72.8 × 101.7 Å in the *x*, *y*, and *z* dimensions contained 158 lipid molecules and 10,746 water molecules. The *z*-direction was perpendicular to the bilayer. Periodic boundary conditions were applied in all three spatial directions. The high-resolution structure 2RLF (residues 23–60) obtained from solution NMR by Schnell et al. (24) served as the starting structure. This structure includes both a transmembrane and an amphiphilic C-terminal helix domain. Five systems were studied in which zero, one, two, three, or all four $His^{37}$ residues were doubly protonated. They were abbreviated M2-0HSP, M2-1HSP, M2-2HSP, M2-3HSP, and M2-4HSP, respectively. The imidazole ring of neutral $His^{37}$ can be protonated at either N$\varepsilon$ or N$\delta$. In accord with NMR experiments (40,44), N$\varepsilon$ was chosen as the preferred protonation site in the simulations unless stated otherwise. In the M2-2HSP system, charged residues were in the diagonal position. A total charge of –1 for the four $Asp^{24}$ residues was used, in accord with previous pKa calculations on this residue in M2 (45). To keep each simulated system neutral, three sodium and 10–14 chloride ions were also included. Phosphate ions were used instead of chloride ions in one simulation of M2-2HSP, as discussed in the text.

Simulations of M2-2HSP initiated from the ssNMR structure (PDB ID 2L0J, residues 22–62) were also carried out. A simulation cell of 88.5 × 88.5 × 130.8 Å containing 224 POPC lipid molecules and 24,285 water molecules was used.

Simulations of M2-3HSP starting from the low-pH x-ray structure (PDB ID 3C9J) were conducted with the protein embedded in a POPC membrane formed by 185 lipids and surrounded by 15,534 water molecules. Three $Na^+$ and five $Cl^-$ ions were also included in the system. The size of the simulation box was 78.4 × 78.4 × 115.0 Å. Although $Gly^{34}$ was mutated to Ala to obtain a better-resolved structure in the x-ray experiment (23), the wild-type protein containing Gly was used in the simulations.

The CHARMM 22 all-atom force field with CMAP (46,47) was applied to describe proteins, with an updated version of potentials for phospholipids (48). The TIP3P model (49) was used for water. The electrostatic interactions were calculated using the particle-mesh Ewald approach with a grid size of 72 × 72 × 100, a cutoff for nonbonded interactions of 12 Å, and a pair list distance of 13.5 Å. Systems were initially relaxed for up to 50–100 ns in the NPT ensemble using the NAMD simulation package (50). After initial equilibration, MD trajectories 2 $\mu$s long, unless specified otherwise in the text, were obtained on the Anton computer at the Pittsburgh Supercomputer Center using the Desmond software package (51). After the initial 100–200 ns in the NPT ensemble, simulations were continued in the NVT ensemble. Temperature was kept at 310 K using the Nosé-Hoover thermostat. The multiple-time-step RESPA algorithm was used with the short and long time steps set to 2 fs and 6 fs using Desmond, and 1 fs and 4 fs using NAMD.

## RESULTS AND DISCUSSION

### Simulated structures of M2 and their comparison with experimental structures

The structures of M2 in all five possible protonation states (M2-0HSP, M2-1HSP, M2-2HSP, M2-3HSP, and M2-4HSP) (see Methods) of $His^{37}$ are stable during the 2 $\mu$s MD trajectories. One of these structures is shown in Fig. 1. Three functionally important residues in the pore are marked in this figure. As can be seen in Fig. 2, the root mean-square deviation (RMSD) of all simulated structures with respect to the initial solution-NMR structure 2RLF remain approximately constant and are <2 Å for

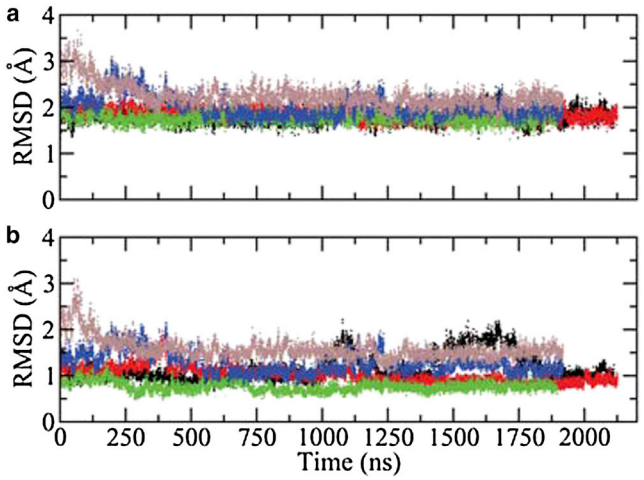


FIGURE 2 RMSDs of backbone atoms in the transmembrane domain (residues 25–46) for M2-0HSP (*black*), M2-1HSP (*red*), M2-2HSP (*green*), M2-3HSP (*blue*), and M2-4HSP (*brown*) as a function of simulation time. (*a*) The simulated structure versus 2RLF. (*b*) The simulated structure versus 3LBW.

the transmembrane backbone atoms. Even smaller values of RMSD are found with respect to the x-ray structure 3LBW, also shown in Fig. 2, and the ssNMR structure 2L0J (not shown). They vary between 1 and 1.5 Å. This reduction is due to the relaxation of helix conformation from the 2RLF to the x-ray and ssNMR structures. The starting structure with a helix tilt angle of ~17° and no kink evolved to a structure with a helix kink of 9° at $Gly^{34}$, a tilt angle of $\theta_1 \sim 34°$ from residues 27 to 34 and $\theta_2 \sim 25°$ from residues 34 to 48. Such tilt angles are in agreement with those of 3LBW ($\theta_1 \sim 30°$,, $\theta_2 \sim 23°$, kink ~7°) and 2L0J ($\theta_1 \sim 29°$, $\theta_2 \sim 21°$, kink ~8°). The structural difference between 2RLF and 3LBW or 2L0J might be attributed to their different nonpolar environments (52): the 2RLF structure was solved in detergent micelles, whereas the 2L0J and the simulated structures were studied in phospholipid bilayers. Among the differently charged states of the channel, M2-2HSP and M2-1HSP most closely resemble the high-resolution experimental structures. The smallest RMSD of only 0.6–0.7 Å is observed between M2-2HSP and 3LBW. The low RMSD values suggest that 3LBW is in a doubly protonated state, which is consistent with nuclear Overhauser effect measurements for this structure (22).

Similarities in RMSD for the five simulated structures do not mean, however, that the channel remains unchanged in response to progressive protonation of $His^{37}$. This can be seen through tracking changes in the pore radius profile, $\overline{r}$. They are plotted in Fig. 3. Of particular interest are effects of protonation on three narrow sites in the pore: 1), the pH sensor $His^{37}$; 2), $Trp^{41}$; and 3), the hydrophobic $Val^{27}$.

At the histidine site, the channel remains narrow in all protonation states, with $\overline{r}$ equal to 0.7, 1.1, 0.8, 1.3, and 1.6 Å as the charge increases from 0 to 4. Even though

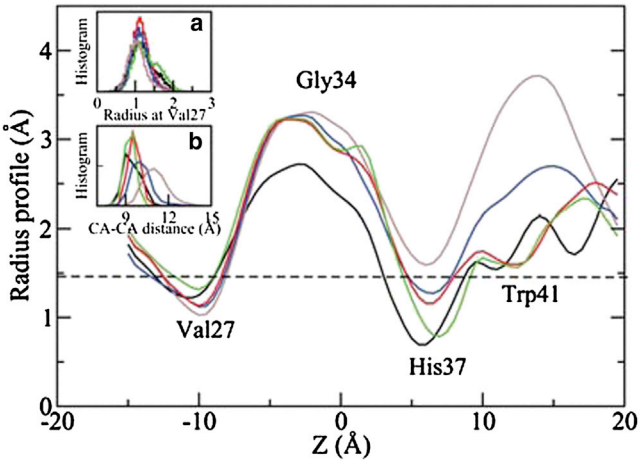


FIGURE 3 Radius profile for M2-0HSP, M2-1HSP, M2-2HSP, M2-3HSP, and M2-4HSP systems (*black*, *red*, *green*, *blue*, and *brown* curves, respectively). The radius is calculated with the aid of the HOLE program (53) and averaged over data from the last 1 $\mu$s of the MD trajectories. The radius of a water molecule is marked by the dashed line. The position of $Gly^{34}$, which is near the center of the POPC membrane, is set at $z = 0$ Å. Positions of $Val^{27}$, $His^{37}$, and $Trp^{41}$ are also marked. (*Inset a*) Histogram of the channel radius at the $Val^{27}$ site. (*Inset b*) Histogram of the distance between $C_\alpha$ atoms of $Trp^{41}$ in neighboring helices. Black, red, green, blue, and brown curves are for 0HSP, 1HSP, 2HSP, 3HSP, and 4HSP systems, respectively. The histograms are based on data averaged over the last 1 $\mu$s of the MD trajectory.

the pore radius increases slightly in high protonated states, it barely reaches the radius of a single water molecule.

At the $Trp^{41}$ site, the channel is narrow only in the M2-0HSP, M2-1HSP, and M2-2HSP systems. The pore radius is equal to 1.5–1.6 Å, which is only slightly above the radius of a water molecule. At higher protonation states, the pore at this site opens up and increases to 2.4 Å in M2-3HSP and even higher, to 3.3 Å, in M2-4HSP. Such behavior suggests that $Trp^{41}$ acts as a pH-sensitive gate, in agreement with physiological experiments by Tang et al. (19), who showed that this residue is responsible for blocking outward proton flux and that its mutations to less bulky residues cause proton leakage.

To probe the reasons for opening the $Trp^{41}$ site, changes in the local backbone structure and the conformation of the indole ring of $Trp^{41}$ were examined. As plotted in Fig. 3 (*inset b*), the distance between the $C_\alpha$ atoms of $Trp^{41}$ on neighboring helices remains approximately the same for M2-0HSP, M2-1HSP, and M2-2HSP, but it increases from 9.0–9.5 Å to 10.1 Å and 13.2 Å upon protonation to M2-3HSP and M2-4HSP, respectively. In contrast, conformation of the $Trp^{41}$ side chain, defined through two torsion angles, $\gamma 1$ and $\gamma 2$, is insensitive to the protonation state of the channel and therefore does not contribute to the opening of the site. The evolution of $\gamma 1$ and $\gamma 2$ with time is shown in Fig. S1 of the Supporting Material. In our simulations, $\gamma 1$ is dominantly in the t-state with its value in the range $180 \pm 30°$. Following the nomenclature in the penultimate rotamer library (54), the indole ring, initially in the t-105 state found in 2RLF, converts to t90 in tens to hundreds of nanoseconds and preferentially occupies this state thereafter, regardless of the protonation state of $His^{37}$. This conformation was also observed in different x-ray structures (3LBW, 3C9J, and 3BKD) (22,23) and identified in ssNMR experiments at both high and low pH (55–58). In agreement with the 3LBW structure, tryptophans interact with $His^{37}$ in an arrangement that is between parallel stacking and a T-shape. Although a stacking conformation between aromatic residues was found mostly at the protein surface, the T-shaped conformation was favored in the hydrophobic core of proteins (59,60). In the M2 channel, the environment containing a few water molecules around $His^{37}$ and $Trp^{41}$ is in between those two, which might explain the intermediate conformation.

The third narrow site in the channel is at $Val^{27}$. The average pore radius at this site is only 1.0–1.3 Å in all protonation states. Due to thermal fluctuations in the structure, the radius also fluctuates. As can be seen in Fig. 3 (*inset a*), the pore radius is larger than the radius of a water molecule only for a fraction of the time (~10%–20%), and only then can water molecules pass through the site. The calculated rate is one molecule/1–2 ns. This suggests that $Val^{27}$ presents a barrier to proton transport, in agreement with recent proton conduction rate measurements by Pielak et al. (17), in which mutation of $Val^{27}$ to a smaller hydrophobic residue yielded an increased proton flux. The significance of $Val^{27}$ as a gate for water transport through the channel was recognized in earlier MD simulations (35,61). However, these simulations were too short to identify the mechanism by which water navigates this gate or to estimate the corresponding free-energy barrier. The barrier to water transfer through the valine valve estimated from the water-density profiles along the pore is 1–2 kcal/mol for M2-0HSP, M2-1HSP, and M2-2HSP but increases to ~3 kcal/mol for M2-3HSP and M2-4HSP. Although these results are in line with the suggestion that water transport through this gate is slower rather than faster at low pH, they are not fully consistent with the model in which the gate is practically shut at high protonation states (22). Also, no large backbone motions that open the $His^{37}$ and close the $Val^{27}$ gate upon protonation, as required by the model, were observed in our simulations or in recent magic-angle-spinning ssNMR experiments (40). In the simulations, the channel remains narrow at both sites. It should be kept in mind that our classical simulations do not provide an estimate of the most relevant quantity—the barrier to proton transfer through the valine gate. This quantity was estimated at 5–10 kcal/mol in calculations based on an empirical valence model (37). In these calculations, however, the structural model of M2 was based on older ssNMR experiments rather than on one of the recent, high-resolution structures.

To gauge whether our results depend on the starting structure, we carried out simulation of the channel in the doubly

protonated state starting with the ssNMR structure 2L0J instead of the solution NMR structure 2RLF. As described in the Supporting Material (Fig. S2), the resulting structure, labeled M2-2HSP-2L0J, is very similar to M2-2HSP. The conformation state of $Trp^{41}$ in both simulated structures is t-90, as in 3LBW. Although the transmembrane helices are quite stable, the C-terminal helices undergo larger fluctuations, as summarized in Fig. S3. The influence of the extramembrane domain on proton transport through M2 appears to be rather limited, however, as experiments with either truncated transmembrane M2 or mutations on the C-terminal helix have shown that the channel retains its proton-conducting activity (7–10,62).

Next, we simulated a triply charged, low-pH structure, labeled M2-3HSP-3C9J, starting from the x-ray structure of the transmembrane domain (residues 22–46; PDB ID 3C9J) at low pH (23). The 3C9J structure differs largely from other structures, with a large span at its C-terminus and a larger helix tilt angle (~38°) compared to that of 20° to 30° in the 2RLF, 3LBW, and 2L0J structures. The RMSD of M2-3HSP-3C9J with respect to the x-ray structure of the same fragment at higher pH (3LBW) is plotted in Fig. S4, as a function of simulation time. Although the RMSD is initially as high as 3.8 Å, the protein backbone relaxes toward the 3LBW structure, eventually yielding an RMSD as small as 1.2 Å. This is similar to the RMSD between M2-3HSP and 3LBW or the solution NMR structure 2RLF (see Fig. 2). This indicates that there is no significant effect of starting structure on the equilibrated MD structure, even if the initial structures markedly differ. One explanation of the difference between M2-3HSP and 3C9J might be that the latter is trapped in a nonequilibrium conformation. Fluctuations in RMSD seen in Fig. S4 *a* correlate with the number of anions near the $His^{37}$-$Trp^{41}$ cage, the positions of which are plotted in Fig. S4 *b*. This is discussed below.

In summary, the data for pore sizes indicate that the M2 channel is closed in the M-0HSP, M2-1HSP, and M2-2HSP states, but opens in the M2-3HSP and M2-4HSP states. This opening is largely due to the increased channel radius at the $Trp^{41}$ site in the latter two structures.

## Important role of anions in maintaining stability of the channel

As discussed above, the $His^{37}$ site is quite narrow even at high protonation states. How are repulsive interactions between the charges on histidines balanced? Our simulations indicate that anions in solution are directly involved in reducing these interactions. In most experimental studies and in the simulations, these were $Cl^-$ anions. In contrast to sodium cations, which are always excluded from the channel, $Cl^-$ anions are absent in the pore only in the unprotonated form of M2. In all charged states, they penetrate the pore, but to different degrees. This can be seen in Fig. 4, where $Cl^-$ ion positions along the channel axis are shown

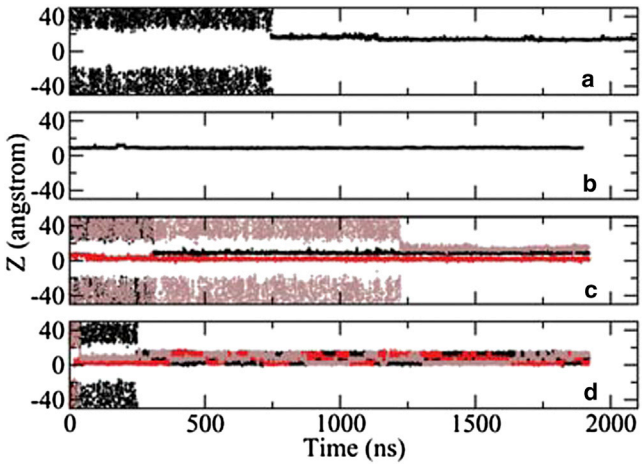


FIGURE 4 Trajectory along the channel axis, $z$, of $Cl^-$ ions that access the pore during the simulation as a function of simulation time. Other $Cl^-$ and $Na^+$ ions do not reside inside the channel and their trajectories are not shown. (*a*) 1HSP. (*b*) 2HSP. (*c*) 3HSP. (*d*) 4HSP. To see this figure in color, go online.

as functions of time. Also, locations of ions from simulation snapshots of M2-2HSP, M2-3HSP, and M2-4HSP are shown in Fig. 5. In M2-1HSP, a single $Cl^-$ ion resides near $Trp^{41}$. In M2-2HSP, electrostatic interactions with two charged histidine residues are sufficiently strong to attract the ion deeper into the pore, such that it occupies space between $His^{37}$ and $Trp^{41}$. This strong attractive interaction makes the structure

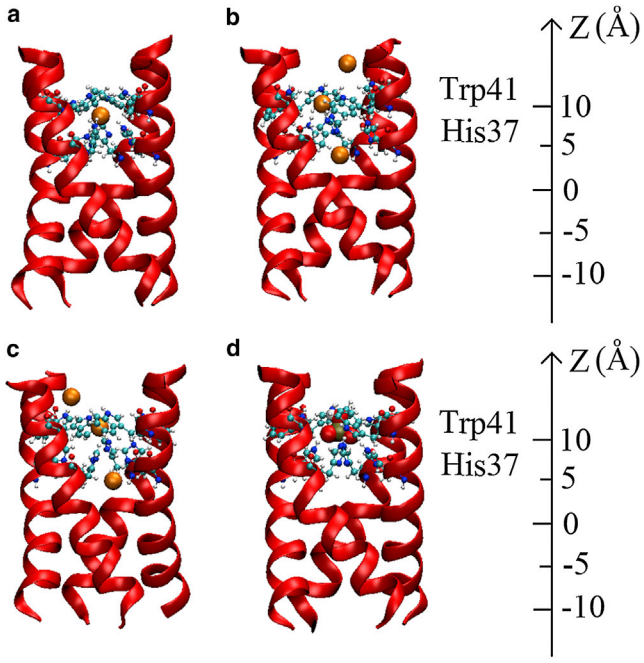


FIGURE 5 Snapshot of M2 (transmembrane domain residues 25–46) from MD simulations for M2-2HSP (*a*), M2-3HSP (*b*), and M2-4HSP (*c*) systems, as well as for M2-2HSP with phosphate anions (*d*). $His^{37}$ and $Trp^{41}$ residues are shown and marked. The $Cl^-$ ions residing in the channel pore are shown as balls (*a–c*). A phosphate anion in the pore is shown in *d*. To see this figure in color, go online.

of M2-2HSP quite compact at the histidine site. The pore size at this site is reduced from 1.1 Å in the M2-1HSP to 0.8 Å despite repulsion between two charged $His^{37}$ residues. At higher protonation states, M2-3HSP and M2-4HSP, additional chloride ions penetrate the pore, blocking the formation of a continuous water wire across the histidine gate. Only in 1% and 2% of M2-3HSP and M2-4HSP structures, respectively, does the transient water wire span the $His^{37}$ gate. Even when the occasional water wire forms, the orientation of water molecules along the wire is rarely conducive to proton transfer, as would be required for proton hopping along a hydrogen-bonded chain. Instead, in most cases, water molecules on both sides of $His^{37}$ point in opposite directions. A similar situation in which an incorrectly oriented chain of water molecules inhibits proton transport was identified in aquaporin channels (63–65). In combination with a small size of the pore at this site, these results suggest that proton transport across the histidine gate proceeds through a different mechanism.

Due to the lack of the exomembrane amphiphilic helix in the M2-3HSP-3C9J system, $Cl^-$ ions diffuse in and out of the channel more easily than in M2-3HSP. As a result, the backbone RMSD increases, as shown in Fig. S4. Increased structural mobility of the truncated channel, compared to the full-length protein, was also observed experimentally (7,8).

To investigate how ion size affects interactions between charged histidines and counterions, we simulated M2-2HSP for 1.5 $\mu$s in the presence of phosphate anions. These ions were present in solution NMR experiments used to determine the 2RLF structure (24). As in the case of $Cl^-$ anions, phosphates are found to bind to positively charged $His^{37}$ sites, as shown in Fig. 5 *d*. This indicates that size and specific chemical nature of counterions are not essential for stabilizing the helical bundle. Ions, however, have to be explicitly present in simulations. When simulations are carried out in the presence of a uniform electrostatic interaction field instead of explicit ions, the helix bundle becomes destabilized in the M2-3HSP and M2-4HSP systems, presumably due to the absence of attraction between charged histidine residues and counterions that would balance electrostatic repulsion between these histidines.

## Conformation of $His^{37}$ residues and their interactions with water: proton transport mechanism

Alternatives to proton transport through the histidine gate via the Grotthuss mechanism are pathways in which $His^{37}$ participates directly in proton translocation. To assess these potential pathways, it is essential to understand conformations and dynamics of the $His^{37}$ side chains and their hydrogen binding characteristics as functions of protonation state of the channel.

It has been argued that a neutral and a charged histidine residue form strong hydrogen bonds that persist on very long timescales (44). This would account for an unusually high pKa value of 8.2 estimated for the first two protonation states of the channel (44). Recently calculated N$\delta$ and N$\varepsilon$ chemical shifts are in agreement with the existence of such bonds (52). However, x-ray structures (22,23) and a later ssNMR study (41) do not support this structural arrangement (66), and neither do recent ab initio MD simulations of the His-Trp tetrad (67). In this study, it has been concluded that the high pKa values for the first two protonation states can be accounted for by cation-$\pi$ interactions between histidine and tryptophan. In our simulations, side chains in the histidine tetrad are highly dynamic, and intermolecular hydrogen bonds in the tetrad are formed only rarely. Although standard classical MD does not reproduce correctly positions of protons shared by nitrogen atoms from two histidines, the energetics of the resulting hydrogen bond and its balance with histidine-water interactions appear to be described correctly. The CHARMM force field (46,47) used in this study yields imidazole-imidazolium and imidazolium-water interaction energies of –21.8 and –15.94 kcal/mol, respectively, in good agreement with corresponding experimentally measured enthalpies of –23.7 and –14.8 kcal/mol (68). It appears that favorable interactions between charged histidines and counterions might contribute to the observed high pKa values.

Conformation of the imidazole ring in histidine can be described by two torsional angles, $\gamma 1$ (N-CA-CB-CG) and $\gamma 2$ (CA-CB-CG-ND). Using the notation from the penultimate rotamer library (54), $His^{37}$ exists mainly in four conformation states: t-160, t-80, t60, and m-70. The first three differ only in their $\gamma 2$ angle, whereas m-70 involves rotations of $\gamma 1$ from 180° to −60° and of $\gamma 2$ from ~165° to ~−70° (compare to t-160). The orientation of the imidazole ring relative to the channel axis depends on its conformational state. In the t-160 and t-80 states, the N$\delta$ proton points toward the extracellular side, whereas in t60 and m-70 the ring is flipped and the same proton points toward the intracellular side. This is illustrated in Fig. 6.

Our further discussion focuses on M2-3HSP and M2-4HSP, which correspond to the open state of the channel. Populations of the four main rotamers at these two protonation states are listed in Table 1. Other conformations,

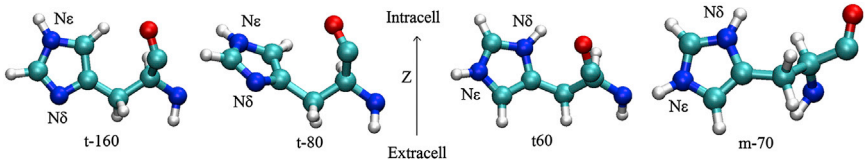


FIGURE 6 Atomic structures of the imidazole ring on $His^{37}$ in ball-and-stick representation in different conformation states. From left to right: t-160, t-80, t60, and m-70. In the first two states, N$\delta$ is on the extracellular side, whereas in the last two, N$\delta$ is on the intracellular side. To see this figure in color, go online.

**TABLE 1 Population of conformations of the imidazole ring of $His^{37}$**

| | M2-3HSP | | M2-4HSP |
|---|---|---|---|
| Conformation | Charged histidine | Neutral histidine | Charged histidine |
| t-160 | 67% | 52% | 52% |
| t-80 | 16% | 46% | 7.8% |
| t60 | 5.6% | 1.4% | 22% |
| m-70 | 9.6% | 0.02% | 16% |

The data are averaged over the last 1 $\mu$s of the MD trajectory and over all $His^{37}$ residues in a given protonation form.

such as p-80, p80, m170, and m80, are populated at <1% and are not listed. Evolution of $\gamma_1$ and $\gamma_2$ with time is plotted in Fig. S5. Neutral $His^{37}$ is found predominantly in the t-160 and t-80 states. In these two states, the N$\delta$ proton is directed toward the extracellular side. In the protonated form, populations of the flipped states, t60 and m-70, increase to 15% and 38% for M2-3HSP and M2-4HSP, respectively. Interconversion between t-160 and t-80 in protonated $His^{37}$ is frequent. These two states are separated by a shallow barrier estimated at 1.5 kcal/mol from the Boltzmann relation, $A(\gamma_2) = kTlnP(\gamma_2)$, between population, $P(\gamma_2)$, and free energy, $A(\gamma_2)$, along $\gamma_2$. Interconversion between the t-160 and t60 states is also fast, with the barrier estimated at 2.7 kcal/mol. A slower dynamics at the submicrosecond scale is found for interconversion between t-160 and m-70 state. Thus, N$\delta$ in protonated $His^{37}$ points toward either the extracellular or intracellular side, whereas in the neutral form it is almost always directed toward the extracellular side.

Both N$\delta$ and N$\varepsilon$ are available to hydrogen-bond with water. The populations of these bonds in different orientations of the imidazole ring are of special interest, because they are expected to correlate with the probability of proton transfer between water and $His^{37}$. They are listed in Table 2. For neutral histidines, frequent hydrogen bonds are observed only for N$\delta$, which points toward the extracelluar side, but not for N$\varepsilon$, which points toward the intracelluar side. In a similar way, N$\delta$ in the charged form is frequently involved in hydrogen bonds with water, but in contrast to neutral histidine, N$\varepsilon$ also interacts with water for an appreciable amount of time. These preferences can be explained by observing that water molecules can readily access the extracellular side of the histidine box and form hydrogen bonds with both charged and uncharged residues. In contrast, only a very few water molecules can access the confined space in the pore between histidines and $Trp^{41}$ on the intracellular side. These molecules preferentially interact with an imidazole ring containing charged rather than uncharged nitrogen atom. The absence of interactions with water in the latter case also helps to stabilize the t-160/t-80 conformation of the side-chain conformation, as it does not disrupt $\pi$-stacking between the imidizaole ring of $His^{37}$ and the indole ring of $Trp^{41}$. The dominance of the t-160/t-80 conformation state makes neutral $His^{37}$ always in position to accept incoming protons. In charged histidines, on the other hand, interactions with water disrupt $\pi$-stacking, yielding a much broader conformation distribution.

Conformational preferences of $His^{37}$ and their interactions with water are consistent with the following mechanism of proton transport across the histidine gate: 1), an incoming proton is transferred to N$\delta$ on a neutral $His^{37}$ that is predominantly in the t-160/t-80 state, and this histidine becomes charged; 2), the imidazole ring of the charged histidine is dynamic and occasionally flips to t60 or m-70; 3), the proton is transferred from N$\delta$ to an intracellular water molecule and the histidine again becomes neutral; and 4), after losing a proton, the neutral histidine flips back to its preferred t-160/t-80 state, in which the N$\delta$ atom is ready to accept an incoming proton. This completes proton transport through the $His^{37}$ gate.

In an alternative route that follows that of the protonation of N$\delta$, the proton on N$\varepsilon$ of a charged $His^{37}$ in the t-160/t-80 conformation is transferred to a water molecule on the intracellular side, This histidine then flips to the t60/m-70 state to accept an incoming proton at the N$\varepsilon$ site. The protonated N$\delta$, which is now on the intracellular side, donates its proton to water. This is followed by the flip to the t-160/t-80 conformation, which completes the cycle. In contrast to the mechanism described previously, in which only protons on N$\delta$ are transferred, protons attached to both N$\delta$ and N$\varepsilon$ cross the gate. To test this mechanism, an additional 1.5 $\mu$s of MD simulation was carried out for an alternative M2-3HSP system in which N$\delta$ rather than N$\varepsilon$ was protonated in the neutral form of $His^{37}$ (labeled as HSD). This represents the state of the system in which the N$\varepsilon$ proton was

**TABLE 2 Populations of hydrogen bonds between water molecules and N$\varepsilon$ or N$\delta$ in different conformations of $His^{37}$ in M2-3HSP and M2-4HSP**

| | M2-3HSP | | M2-4HSP |
|---|---|---|---|
| Conformation | Charged histidine N$\varepsilon$-H$\cdots$O; N$\delta$-H$\cdots$O | Neutral histidine, N$\varepsilon$-H$\cdots$O; N$\delta\cdots$H-O-H | Charged histidine, N$\varepsilon$-H$\cdots$O; N$\delta$-H$\cdots$O |
| t-160 | 34%; 69% | 0.5%; 81% | 63%; 62% |
| t-80 | 37%; 88% | 0.2%; 64% | 59%; 79% |
| t60 | 27%; 78% | 0% | 26%; 83% |
| m-70 | 56%; 93% | 0% | 70%; 94% |

The following criteria for hydrogen bonds are used: N$\cdots$O < 3.5 Å and H$\cdots$O < 2.5 Å in the case of N–H$\cdots$O; N$\cdots$O < 3.5 Å and N$\cdots$H < 2.5 Å in the case of N$\cdots$H–O. The data are averaged over the last 1 $\mu$s of the MD trajectory and over all $His^{37}$ residues in a given protonation form.

transferred to water. The HSD side chain is found to be quite dynamic, with a broad conformation distribution: 17% in t-160, 5% in t-80, 43% in t60, 5% in m-70, 6% in m170, and 24% in m80. Among these states, only in m-70 N$\varepsilon$ of HSD is orientated to accept an incoming proton from the extracellular side needed to complete the proton transport cycle. Considering that the population of m-70 is only 5%, of which N$\varepsilon$ forms hydrogen bonds with water only 26% of the time, this alternative route is expected to be quite inefficient.

Strong interactions between water molecules and $His^{37}$ were observed in recent ssNMR experiments in which the on and off rates of proton transfer were estimated to be at the submicrosecond to microsecond timescale (41). Earlier ssNMR experiments (40) also indicate that conformational transitions in $His^{37}$ occur at the microsecond timescale. These transitions were interpreted as rotations between t-160 and a nearby state shifted in $\gamma_2$ by 40°. However, it is not clear what type of structural constraints might yield two minima separated by a relatively high barrier that are located so close along a single rotational angle. MD simulations indicate that rotations involving only $\gamma 2$ are rather fast and occur at a nanosecond scale. Slow interconversions, at the submicrosecond timescale, involve large rotational changes in both $\gamma 1$ and $\gamma 2$, such as transitions between t-160 and m-70. It seems that these conformational transitions were not included in the analysis of REDOR signals obtained from the ssNMR experiment (40).

In addition to the shutter and shuttle mechanisms, another model that involves large conformational change of the channel upon protonation of $His^{37}$ was also proposed on the basis of x-ray structures obtained at neutral (23,24) and low pH (24). In this model, the channel opens up alternatively at $Val^{27}$ at high or neutral pH and at $His^{37}$ at low pH. Our MD simulations show rather stable backbone structures in all protonation states of $His^{37}$ without any large conformational changes, and the channel remains narrow at both $His^{37}$ and $Val^{27}$ site. The recent ssNMR experiment by Hu et al. (41) also found no large backbone conformation changes that would be required in the model. However, in partial support of the model, we observed the tightening of the valine site at the high protonation states.

MD simulation studies rely on the accuracy of empirical force fields. The CHARMM force field applied here has been used to understand the structure and function of M2 in a number of previous studies (22,42,70,71). The close agreement between the structures simulated in this study and the high-resolution x-ray or NMR structures regarding helix tilt and kink angle, side-chain conformations, and the relative orientation of $His^{37}$ and $Trp^{41}$ suggests that the force field properly descibes the system. The situation is less clear with other force fields. Simulations carried out with the aid of the GROMOS87 force field yielded a less satisfactory agreement with experiments (61). In particular, several MD trajectories initiated from the ssNMR structure 1NYJ and the solution NMR structure 2RLF for the doubly or triply protonated M2 led water wires spanning the $His^{37}$-$Trp^{41}$ region. The simulations, however, were approximately two orders of magnitude shorter than those described here, and as the authors point out, the results depended on the starting structure.

In the presence of excess protons, delocalization of charges could be important in the $His^{37}$-$Trp^{41}$ region. However, a recent ab initio study on His-Trp cluster showed no sigificiant charge transfer between His and Trp residues (67), which justifies the use of point charges for electrostatics interactions. Previous modeling studies have shown that ab initio calculations and calculations based on CHARMM potentials yield similar binding energies and distances for stacked or T-shaped His-Trp clusters found in different experimental structures (72). A comparison with ab initio calculations led to the conclusion that the empirical potential is adequate to describe cation-$\pi$ interactions between a point charge and an indole ring (73). This is the main contribution to the interaction between protonated His and the Trp side chain. These studies suggest that classical MD simulations are suitable for describing the structure of the functionally important $His^{37}$-$Try^{41}$ cluster. Even though charge delocailztion between $His^{37}$ and $Trp^{41}$ might be limited, transfer of a proton from $His^{37}$ to nearby water molecules is expected to be essential for proton conductance, a process that cannot be described by empirical force fields.

## CONCLUSIONS

Extensive MD simulations at theh microsecond timescale are used to investigate the activation process and proton transport mechanism in the M2 channel. The channel is shown to exist in the closed state in 0HSP, 1HSP, and 2HSP protonation states of $His^{37}$. The M2-2HSP system closely resembles the x-ray structure of M2 (PDB ID 3LBW) obtained at pH 6.5. With further protonation of the histidine to the 3HSP and 4HSP states, the site at $Trp^{41}$ residue opens with an enlarged channel radius due to increased distance between the neighboring helix backbones, attributed to the electrostatic repulsion between charged histidine residues. Anions present in the system are shown to access the positively charged $His^{37}$ site in the high protonation states to stabilize the channel and block the formation of a continuous water wire at $His^{37}$. Detailed analysis shows that transport through $His^{37}$ involves proton transfer to and from this residue, correlated with interconversion between different conformation states of its side chain. The valve at $Val^{27}$ becomes somewhat narrower as pH decreases, giving partial support to the model recently proposed by Khurana et al. (42) and Acharya et al. (22), but large, structural changes involved in this model have not been observed.

## SUPPORTING MATERIAL

One table and five figures are available at http://www.biophysj.org/biophysj/supplemental/S0006-3495(13)00977-6.

The authors thank the Pittsburgh Supercomputer Center for providing computer time that facilitated this work.

This work was supported by the NASA Exobiology Program.

## REFERENCES

1. Pinto, L. H., L. J. Holsinger, and R. A. Lamb. 1992. Influenza virus $M_2$ protein has ion channel activity. *Cell.* 69:517–528.
2. Chizhmakov, I. V., F. M. Geraghty, …, A. J. Hay. 1996. Selective proton permeability and pH regulation of the influenza virus M2 channel expressed in mouse erythroleukaemia cells. *J. Physiol.* 494:329–336.
3. Shimbo, K., D. L. Brassard, …, L. H. Pinto. 1996. Ion selectivity and activation of the M2 ion channel of influenza virus. *Biophys. J.* 70:1335–1346.
4. Mould, J. A., J. E. Drury, …, L. H. Pinto. 2000. Permeation and activation of the M2 ion channel of influenza A virus. *J. Biol. Chem.* 275:31038–31050.
5. Jackson, D., A. Cadman, …, W. S. Barclay. 2002. A reverse genetics approach for recovery of recombinant influenza B viruses entirely from cDNA. *J. Virol.* 76:11744–11747.
6. Takeda, M., A. Pekosz, …, R. A. Lamb. 2002. Influenza A virus $M_2$ ion channel activity is essential for efficient replication in tissue culture. *J. Virol.* 76:1391–1399.
7. Tobler, K., M. L. Kelly, …, R. A. Lamb. 1999. Effect of cytoplasmic tail truncations on the activity of the $M_2$ ion channel of influenza A virus. *J. Virol.* 73:9695–9701.
8. Ma, C., A. L. Polishchuk, …, L. H. Pinto. 2009. Identification of the functional core of the influenza A virus A/M2 proton-selective ion channel. *Proc. Natl. Acad. Sci. USA.* 106:12283–12288.
9. Salom, D., B. R. Hill, …, W. F. DeGrado. 2000. pH-dependent tetramerization and amantadine binding of the transmembrane helix of M2 from the influenza A virus. *Biochemistry.* 39:14160–14170.
10. Hu, J., R. Fu, and T. A. Cross. 2007. The chemical and dynamical influence of the antiviral drug amantadine on the M2 proton channel transmembrane domain. *Biophys. J.* 93:276–283.
11. Pinto, L. H., G. R. Dieckmann, …, W. F. DeGrado. 1997. A functionally defined model for the M2 proton channel of influenza A virus suggests a mechanism for its ion selectivity. *Proc. Natl. Acad. Sci. USA.* 94:11301–11306.
12. Nishimura, K., S. Kim, …, T. A. Cross. 2002. The closed state of a $H^+$ channel helical bundle combining precise orientational and distance restraints from solid state NMR. *Biochemistry.* 41:13170–13177.
13. Lin, T.-I., and C. Schroeder. 2001. Definitive assignment of proton selectivity and attoampere unitary current to the M2 ion channel protein of influenza A virus. *J. Virol.* 75:3647–3656.
14. Chizhmakov, I. V., D. C. Ogden, …, A. J. Hay. 2003. Differences in conductance of M2 proton channels of two influenza viruses at low and high pH. *J. Physiol.* 546:427–438.
15. Vijayvergiya, V., R. Wilson, …, D. D. Busath. 2004. Proton conductance of influenza virus M2 protein in planar lipid bilayers. *Biophys. J.* 87:1697–1704.
16. Moffat, J. C., V. Vijayvergiya, …, D. D. Busath. 2008. Proton transport through influenza A virus M2 protein reconstituted in vesicles. *Biophys. J.* 94:434–445.
17. Pielak, R. M., and J. J. Chou. 2010. Kinetic analysis of the M2 proton conduction of the influenza virus. *J. Am. Chem. Soc.* 132:17695–17697.
18. Wang, C., R. A. Lamb, and L. H. Pinto. 1995. Activation of the M2 ion channel of influenza virus: a role for the transmembrane domain histidine residue. *Biophys. J.* 69:1363–1371.
19. Tang, Y., F. Zaitseva, …, L. H. Pinto. 2002. The gate of the influenza virus M2 proton channel is formed by a single tryptophan residue. *J. Biol. Chem.* 277:39880–39886.
20. Venkataraman, P., R. A. Lamb, and L. H. Pinto. 2005. Chemical rescue of histidine selectivity filter mutants of the M2 ion channel of influenza A virus. *J. Biol. Chem.* 280:21463–21472.
21. Pielak, R. M., J. R. Schnell, and J. J. Chou. 2009. Mechanism of drug inhibition and drug resistance of influenza A M2 channel. *Proc. Natl. Acad. Sci. USA.* 106:7379–7384.
22. Acharya, R., V. Carnevale, …, M. L. Klein. 2010. Structure and mechanism of proton transport through the transmembrane tetrameric M2 protein bundle of the influenza A virus. *Proc. Natl. Acad. Sci. USA.* 107:15075–15080.
23. Stouffer, A. L., R. Acharya, …, W. F. DeGrado. 2008. Structural basis for the function and inhibition of an influenza virus proton channel. *Nature.* 451:596–599.
24. Schnell, J. R., and J. J. Chou. 2008. Structure and mechanism of the M2 proton channel of influenza A virus. *Nature.* 451:591–595.
25. Sharma, M., M. Yi, …, T. A. Cross. 2010. Insight into the mechanism of the influenza A proton channel from a structure in a lipid bilayer. *Science.* 330:509–512.
26. Pielak, R. M., and J. J. Chou. 2010. Solution NMR structure of the V27A drug resistant mutant of influenza A M2 channel. *Biochem. Biophys. Res. Commun.* 401:58–63.
27. Cady, S. D., K. Schmidt-Rohr, …, M. Hong. 2010. Structure of the amantadine binding site of influenza M2 proton channels in lipid bilayers. *Nature.* 463:689–692.
28. Sansom, M. S., I. D. Kerr, …, H. S. Son. 1997. The influenza A virus M2 channel: a molecular modeling and simulation study. *Virology.* 233:163–173.
29. von Grotthuss, C. J. T. 1806. Sur la décomposition de l'eau et des corps qu'elle tient en dissolution à l'aide de l'électricité galvanique. *Ann. Chim.* 58:54–74.
30. Agmon, N. 1995. The Grotthuss mechanism. *Chem. Phys. Lett.* 244:456–462.
31. Smondyrev, A. M., and G. A. Voth. 2002. Molecular dynamics simulation of proton transport through the influenza A virus M2 channel. *Biophys. J.* 83:1987–1996.
32. Hung, A., K. Tai, and M. S. Sansom. 2005. Molecular dynamics simulation of the M2 helices within the nicotinic acetylcholine receptor transmembrane domain: structure and collective motions. *Biophys. J.* 88:3321–3333.
33. Wu, Y., and G. A. Voth. 2005. A computational study of the closed and open states of the influenza a M2 proton channel. *Biophys. J.* 89:2402–2411.
34. Kass, I., and I. T. Arkin. 2005. How pH opens a $H^+$ channel: the gating mechanism of influenza A M2. *Structure.* 13:1789–1798.
35. Yi, M., T. A. Cross, and H.-X. Zhou. 2008. A secondary gate as a mechanism for inhibition of the M2 proton channel byamantadine. *J. Phys. Chem. B Lett.* 112:7977–7979.
36. Yi, M., T. A. Cross, and H.-X. Zhou. 2009. Conformational heterogeneity of the M2 proton channel and a structural model for channel activation. *Proc. Natl. Acad. Sci. USA.* 106:13311–13316.
37. Chen, H., Y. Wu, and G. A. Voth. 2007. Proton transport behavior through the influenza A M2 channel: insights from molecular simulation. *Biophys. J.* 93:3470–3479.
38. Lear, J. D. 2003. Proton conduction through the M2 protein of the influenza A virus; a quantitative, mechanistic analysis of experimental data. *FEBS Lett.* 552:17–22.
39. Schweighofer, K. J., and A. Pohorille. 2000. Computer simulation of ion channel gating: the $M_2$ channel of influenza A virus in a lipid bilayer. *Biophys. J.* 78:150–163.
40. Hu, F., W. Luo, and M. Hong. 2010. Mechanisms of proton conduction and gating in influenza M2 proton channels from solid-state NMR. *Science.* 330:505–508.

41. Hu, F., K. Schmidt-Rohr, and M. Hong. 2012. NMR detection of pH-dependent histidine-water proton exchange reveals the conduction mechanism of a transmembrane proton channel. *J. Am. Chem. Soc.* 134:3703–3713.

42. Khurana, E., M. Dal Peraro, …, M. L. Klein. 2009. Molecular dynamics calculations suggest a conduction mechanism for the M2 proton channel from influenza A virus. *Proc. Natl. Acad. Sci. USA*. 106:1069–1074.

43. Okada, A., T. Miura, and H. Takeuchi. 2001. Protonation of histidine and histidine-tryptophan interaction in the activation of the M2 ion channel from influenza A virus. *Biochemistry.* 40:6053–6060.

44. Hu, J., R. Fu, …, T. A. Cross. 2006. Histidines, heart of the hydrogen ion channel from influenza A virus: toward an understanding of conductance and proton selectivity. *Proc. Natl. Acad. Sci. USA*. 103: 6865–6870.

45. Forrest, L. R., A. Kukol, …, M. S. P. Sansom. 2000. Exploring models of the influenza A M2 channel: MD simulations in a phospholipid bilayer. *Biophys. J.* 78:55–69.

46. MacKerell, Jr., A. D., D. Bashford, …, M. Karplus. 1998. All-atom empirical potential for molecular modeling and dynamics studies of proteins. *J. Phys. Chem. B.* 102:3586–3616.

47. Mackerell, Jr., A. D., M. Feig, and C. L. I. I. I. Brooks, 3rd. 2004. Extending the treatment of backbone energetics in protein force fields: limitations of gas-phase quantum mechanics in reproducing protein conformational distributions in molecular dynamics simulations. *J. Comput. Chem.* 25:1400–1415.

48. Klauda, J. B., R. M. Venable, …, R. W. Pastor. 2010. Update of the CHARMM all-atom additive force field for lipids: validation on six lipid types. *J. Phys. Chem. B.* 114:7830–7843.

49. Jorgensen, W. L., J. Chandrasekhar, …, M. L. Klein. 1983. Comparison of simple potential functions for simulating liquid water. *J. Chem. Phys.* 79:926–935.

50. Phillips, J. C., R. Braun, …, K. Schulten. 2005. Scalable molecular dynamics with NAMD. *J. Comput. Chem.* 26:1781–1802.

51. Shaw, D. E., R. O. Dror, …, B. Towles. 2009. Millisecond-scale molecular dynamics simulations on Anton. *Proc.. Conf. High Perform. Comput. Supercomput., Network., Storage Anal,, Portland, Oregon.*

52. Dong, H., M. Yi, …, H.-X. Zhou. 2013. Ab initio calculations and validation of the pH-dependent structures of the $His^{37}$-$Trp^{41}$ quartet, the heart of acid activation and proton conductance in the M2 protein of Influenza A virus. *Chem Sci.* 4:2776–2787.

53. Smart, O. S., J. M. Goodfellow, and B. A. Wallace. 1993. The pore dimensions of gramicidin A. *Biophys. J.* 65:2455–2460.

54. Lovell, S. C., J. M. Word, …, D. C. Richardson. 2000. The penultimate rotamer library. *Proteins.* 40:389–408.

55. Luo, W., R. Mani, and M. Hong. 2007. Side-chain conformation of the M2 transmembrane peptide proton channel of influenza a virus from $^{19}F$ solid-state NMR. *J. Phys. Chem. B.* 111:10825–10832.

56. Witter, R., F. Nozirov, …, R. Fu. 2008. Solid-state $^{19}F$ NMR spectroscopy reveals that $Trp^{41}$ participates in the gating mechanism of the M2 proton channel of influenza A virus. *J. Am. Chem. Soc.* 130:918–924.

57. Witter, R., R. Fu, …, A. S. Ulrich. 2010. Solid-state $^{15}N$-NMR investigations on the pH dependent conformation of Trp-41 of the M2 proton channel of influenza A virus in advances. *In* Biomedical Research. P. Anninos, M. Rossi, T. D. Pham, C. Falugi, A. Bussing, and M. Koukkou, editors. WSEAS Press, Athens, Greece, pp. 277–283.

58. Williams, J. K., Y. Zhang, …, M. Hong. 2013. pH-dependent conformation, dynamics, and aromatic interaction of the gating tryptophan residue of the influenza M2 proton channel from solid-state NMR. *Biophys. J.* 104:1698–1708.

59. Burley, S. K., and G. A. Petsko. 1985. Aromatic-aromatic interaction: a mechanism of protein structure stabilization. *Science.* 229:23–28.

60. Mitchell, J. B. O., C. L. Nandi, …, S. L. Price. 1994. Amino/aromatic interactions in proteins: is the evidence stacked against hydrogen bonding? *J. Mol. Biol.* 239:315–331.

61. Leonov, H., and I. T. Arkin. 2009. Structure and dynamics of the influenza A M2 channel: a comparison of three structures. *J. Mol. Model.* 15:1317–1328.

62. Stewart, S. M., and A. Pekosz. 2011. Mutations in the membrane-proximal region of the influenza A virus M2 protein cytoplasmic tail have modest effects on virus replication. *J. Virol.* 85:12179–12187.

63. Murata, K., K. Mitsuoka, …, Y. Fujiyoshi. 2000. Structural determinants of water permeation through aquaporin-1. *Nature.* 407:599–605.

64. Tajkhorshid, E., P. Nollert, …, K. Schulten. 2002. Control of the selectivity of the aquaporin water channel family by global orientational tuning. *Science.* 296:525–530.

65. Kosinska Eriksson, U., G. Fischer, …, R. Neutze. 2013. Subangstrom resolution x-ray structure details aquaporin-water interactions. *Science.* 340:1346–1349.

66. Hong, M., and W. F. DeGrado. 2012. Structural basis for proton conduction and inhibition by the influenza M2 protein. *Prot. Sci.* 21:1620–1633.

67. Bankura, A., M. L. Klein, and V. Carnevale. 2013. Proton affinity of the histidine-tryptophan cluster motif from the influenza A virus from ab initio molecular dynamics. *Chem. Phys.* 422:156–164.

68. Mautner, M. 1988. Models for strong interactions in proteins and enzymes. 2. Interactions of ions with the peptide link and with imidazole. *J. Am. Chem. Soc.* 110:3075–3080.

69. Reference deleted in proof.

70. Khurana, E., R. H. Devane, …, M. L. Klein. 2011. Computational study of drug binding to the membrane-bound tetrameric M2 peptide bundle from influenza A virus. *Biochim. Biophys. Acta.* 1808:530–537.

71. Wang, J., C. Ma, G. Fiorin, V. Carnevale, T. Wang, F. Hu, R. A. Lamb, L. H. Pinto, M. Hong, M. L. Klein, and W. F. DeGrado. 2011. Molecular dynamics simulation directed rational design of inhibitors targeting drug-resistant mutants of influenza A virus M2. *J. Am. Chem. Soc.* 133:12834–12841.

72. Alagona, G., C. Ghio, …, S. Monti. 1999. Theoretical investigation of histidine-tryptophan preferential interactions. *Theor. Chem. Acc.* 101:143–150.

73. Woolf, T. B., A. Grossfield, and J. G. Pearson. 1999. Indoles at interfaces: calculations of electrostatic effects with density functional and molecular dynamics methods. *Int. J. Quantum Chem.* 75:197–206.